Flow and Mixing in the Rift Valley of the Mid-Atlantic Ridge

A. M. THURNHERR

Department of Oceanography, The Florida State University, Tallahassee, Florida

K. J. RICHARDS

School of Ocean and Earth Science, Southampton Oceanography Centre, Southampton, United Kingdom

C. R. GERMAN

Challenger Division, Southampton Oceanography Centre, Southampton, United Kingdom

G. F. LANE-SERFF

Department of Civil and Construction Engineering, UMIST, Manchester, United Kingdom

K. G. SPEER

Department of Oceanography, The Florida State University, Tallahasse, Florida

(Manuscript received 3 July 2001, in final form 18 October 2001)

ABSTRACT

High levels of diapycnal mixing and geothermal heating near midocean ridges contribute to the buoyancy fluxes that are required to close the global circulation. In topographically confined areas, such as the deep median valleys of slow-spreading ridges, these fluxes strongly influence the local hydrography and dynamics. Data from a segment-scale hydrographic survey of the rift valley of the Mid-Atlantic Ridge and from an array of current meters deployed there during an entire year are analyzed in order to characterize the dominant hydrographic patterns and dynamical processes. Comparison with historic hydrographic data indicates that the temporal variability during the last few decades has been small compared to the observed segment-scale gradients. The rift valley circulation is characterized by inflow from the eastern ridge flank and persistent unidirectional along-segment flow into a cul-de-sac. Therefore, most of the water flowing along the rift valley upwells within the segment with a mean vertical velocity $>10^{-5}$ m s^{-1}. The observed streamwise hydrographic gradients indicate that diapycnal mixing dominates the rift valley buoyancy fluxes by more than an order of magnitude, in spite of the presence of a large hydrothermal vent field supplying several gigawatts of heat to the water column. Hydrographic budgets in the rift valley yield diffusivity values of order 5×10^{-3} m^2 s^{-1}, consistent with estimates derived from statically unstable overturns, the largest of which were observed downstream of topographic obstacles in the path of the along-segment flow. This suggests vertical shear associated with cross-sill flows as the dominant contributor to the mechanical mixing in the rift valley.

1. Introduction

The midocean ridge system, which spans the entire globe with a total length of approximately 60×10^3 km, marks the constructive boundaries between tectonic plates where the cooling of recently formed lithosphere accounts for a large portion of the geothermal heat flux to the oceans (e.g., Stein and Stein 1994). Midocean ridges, especially slow-spreading ones such as the Mid-Atlantic Ridge (MAR), are characterized by rough topography that is associated with greatly enhanced levels of diapycnal mixing in comparison to the much smoother abyssal plains and continental slopes (Polzin et al. 1997). Both geothermal heating and diapycnal mixing contribute to the buoyancy flux, which is required in a steady-state circulation to balance the heat lost to the atmosphere during the formation of deep water at high latitudes. [While it is often assumed that the geothermal contribution is negligible on a global scale, recent modeling work by Adcroft et al. (2001) indicates that this view may not be entirely correct.] These considerations suggest that the midocean ridge system may be of fundamental importance for the global circulation.

There are at least two processes known to enhance

Corresponding author address: A. M. Thurnherr, Dept. of Oceanography, The Florida State University, Tallahassee, FL 32306-4320. E-mail: A.Thurnherr@ocean.fsu.edu.

diapycnal mixing in the vicinity of rough topography: breaking internal waves and (hydraulically controlled) cross-sill flows. From the spatial distribution of microstructure observations over the flank of the MAR in the South Atlantic Polzin et al. (1997) inferred that the observed enhancement of diapycnal mixing is related to breaking internal waves, most likely generated by tidal flows interacting with the topography. A global energy budget supports the notion that a significant portion of the energy required for mixing can be derived from tidal–topographic interactions (Munk and Wunsch 1998). Observations from hydraulically controlled exchange flows and overflows connecting major ocean basins also indicate greatly enhanced mixing (e.g., Wesson and Gregg 1994; Ferron et al. 1998), but the question if similar processes acting on smaller scales can contribute significantly to regional buoyancy fluxes does not appear to have been investigated yet.

It has been hypothesized that canyons on the flanks of midocean ridges are locations where diapycnal fluxes are concentrated (St. Laurent et al. 2001). Rift valleys, which are primarily associated with slow plate-spreading rates, have not received much attention in this context. The primary goal of our study is an investigation of the segment-scale hydrography and dynamics in the rift valley of two connected segments of the MAR, with emphasis on the diapycnal fluxes. In the remainder of the introduction relevant prior work is reviewed. The study site and datasets are presented in section 2; this is followed by a characterization of the segment-scale hydrography (section 3) and by current-meter transport calculations (section 4). The observations indicate persistent unidirectional along-valley flow down a horizontal density gradient, which requires a diapycnal buoyancy flux dwarfing that of a local hydrothermal vent field (section 5). Estimates of the diapycnal diffusivities in the rift valley calculated from unstable overturns (section 6) are consistent with budget-derived values, and their spatial distribution suggests that much of the mixing is associated with flows across sills partially blocking the rift valley. The observations are discussed in section 7.

Apparently the first systematic study of the hydrography in the rift valley of the MAR was carried out by Fehn et al. (1977), who analyze temperature observations from 47 stations occupied 1972–74 in two segments between 36.5° and 37°N, overlapping with the northern end of our study area (section 2). They find the rift valley water column to be weakly stratified in comparison to nearby profiles on the ridge flanks and observe a monotonic along-segment temperature gradient of $\approx 5 \times 10^{-3}$ °C km^{-1}, which they attribute to inflows of different densities at the two segment ends. On the basis of the expected magnitudes of geothermal temperature anomalies in the water column Fehn et al. (1977) conclude that geothermal heating does not contribute significantly to the observed patterns. They furthermore note that their data is fully consistent with temperature profiles taken in the same segments in 1959 and 1964, that is, the rift valley hydrography appears to be stable on a timescale of years.

Saunders and Francis (1985) also analyze rift valley temperature data. Their 27 profiles from 7 segments between 43° and 47°N indicate that monotonic along-valley gradients are common. Their longest segment is characterized by a bottom-temperature gradient of order 0.8×10^{-3} °C km^{-1}. In contrast to Fehn et al. (1977) the model for rift valley ventilation of Saunders and Francis (1985) consists of hydraulically controlled inflow across the deepest sill only. They discuss a number of different processes that can provide the density flux within a segment to balance the inflow and conclude that the most likely scenario consists of alternating inflow events and periods of homogenization caused by diapycnal mixing (tidal stirring). Similar to Fehn et al. (1977) they discount geothermal heating as a primary cause for the observed hydrographic patterns.

Wilson et al. (1995) include salinity data in their study of the hydrography within (and overlying) the rift valley of the MAR between 33° and 40°N. Their measurements indicate that the rift valley hydrography is complicated by numerous lateral intrusions that obscure possible signatures of geothermal heating. Their sections show indications for along-valley sloping isotherms and isopycnals, most notably between 35.6° and 37.1°N, which covers the segments investigated by Fehn et al. (1977) and in our study.

On a smaller scale Thurnherr and Richards (2001) analyze hydrographic and velocity data near 36.25°N, where the rift valley is partially blocked by a sill. Their data indicate that the local dynamics are dominated by a hydraulically controlled, persistent (during 3 weeks), unidirectional (northeastward) flow across the sill. A hydrothermal vent field 5 km upstream of the sill provides a heat flux of ≈3 GW to the rift valley water column without significantly affecting the dynamics. The maximum observed temperature anomalies associated with the neutrally buoyant hydrothermal particle plume are -5×10^{-3} °C; the plume is cold/fresh as expected in the deep Atlantic where the background salinity stratification is unstable (cf. McDougall 1990).

The majority of the available velocity data from the rift valley of the MAR were recorded by current meters moored in the vicinity of hydrothermal vent fields (e.g., Rudnicki et al. 1994; Lukashin et al. 1995; Jean-Baptiste et al. 1998; Murton et al. 1999). An exception are the velocities presented by Keller et al. (1975), which were recorded during 46 days of mooring deployment near 36.75°N in 1973. These measurements are of particular interest here because they were made in the next segment north of our study area, that is, in the segment investigated by Fehn et al. (1977). Two fully functional instruments recorded semidiurnal tidal currents of 0.03–0.04 m s^{-1}, superimposed on mean velocities of 0.03 m s^{-1} and 0.08 m s^{-1}; that is, the flow recorded by one of the two instruments was persistent and unidirectional

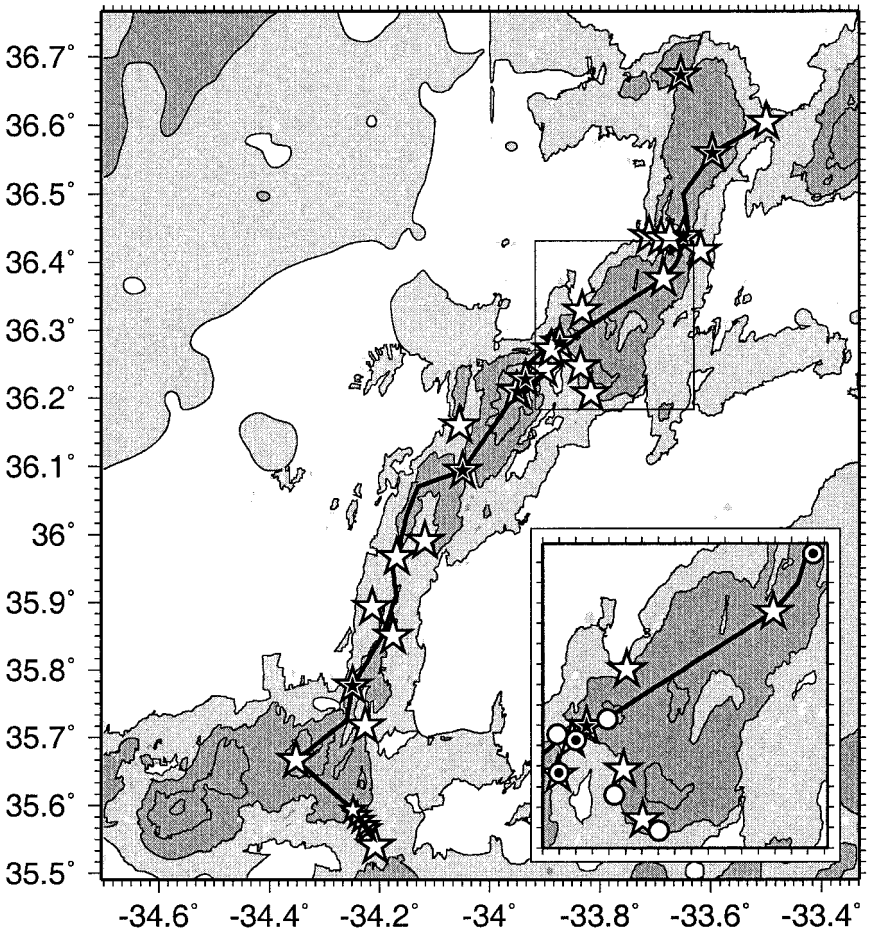

FIG. 1. AMAR bathymetry, CTD stations (stars), and current-meter moorings (circles, inset only). Shaded areas are deeper than 2000 m in the mosaic of the datasets of Needham et al. (1992) and of Smith and Sandwell (1997) (version 6.2); dark shading indicates depth >2500 m; contours are drawn every 500 below 2000 m. The heavy line marks the deepest axis of the rift valley. Black stars with white borders indicate profiles with linear θ_2/S characteristics extending below 2550 m; small stars near 35.55°N, 34.2°W show the bottom turning points of a CTD tow-yo. The moorings marked with bullets are used to illustrate the along-segment evolution of the rift valley flow. The box in the main panel indicates the location of the inset.

(northeastward) along the segment, as opposed to the apparently more common situation of tidal dominance (e.g., Rudnicki et al. 1994; Lukashin et al. 1995; Jean-Baptiste et al. 1998). An instrument on a different mooring that recorded only directional data provides additional evidence for unidirectional flow and similar northeastward flows had been observed during several further short deployments in the same segment in another year (Keller et al. 1975). Spectral analysis of the 1973 data shows significant energy in the near-inertial, semidiurnal and diurnal tidal bands as well as at nonlinear interaction frequencies, similar to observations near a midocean ridge elsewhere (Mihaly et al. 1998).

2. Data

Figure 1 shows the bathymetry of the two AMAR (ALVIN Mid-Atlantic Ridge) segments and the locations of the conductivity–temperature–depth (CTD) stations and current-meter moorings used in this study. The rift valley runs from the southwest (SW) to the northeast (NE). The lateral offset where the rift valley is partially blocked by a bathymetric high near 36.25°N (detailed view in inset) is a nontransform discontinuity separating the ridge into two segments: AMAR in the NE and South AMAR in the SW. The approximate lengths of the two segments are 100 km (South AMAR) and 50 km (AMAR). [Detrick et al. (1995) further subdivide South AMAR into three segments (PO-5, PO-6, and PO-7 in their terminology); PO-5 was previously called AMAR Minor, but subsequent sidescan sonar investigation has revealed no magmatic evidence to support this distinction as a separate segment (Parson et al. 2000).] The rift valley floor is characterized by a number of deep ''basins'' (defined here as depressions below 2500 m) connected by shallower ''sills.'' On both sides of the

valley the walls rise to depths above 2000 m. Below 2000 m there is a sill connecting South AMAR to the North Oceanographer segment near 35.6°N, 34.6°W (minimum depth 2200 m). North of AMAR the rift valley continues in the FAMOUS segment, studied by Keller et al. (1975) and by Fehn et al. (1977), which is connected to AMAR by the sill near 36.6°N, 33.5°W (minimum depth 2200 m). The deepest sill of the segments near 35.55°N, 34.2°W (minimum depth 2300 m) connects South AMAR to the eastern ridge flank.

In June–July 1998 the AMAR segments were visited during the *FLAME-2* cruise, the main purpose of which was the recovery of eight moorings with 25 current meters deployed there in 1997. [The hydrographic data from the 1997 cruise are analyzed in detail by Thurnherr and Richards (2001).] One mooring was lost; the locations of the remaining ones with 21 current meters are indicated by circles in the inset of Fig. 1. The stars mark the locations of a tow-yo (small stars near 35.55°N, 34.2°W) and of 29 full-depth CTD stations occupied during 6 days of sampling. Additionally, an eastern off-ridge background station of the 1997 cruise (≈50 km off axis) was reoccupied for reference. Calibration data indicate accuracies of the temperature and salinity measurements of 1.5×10^{-3} °C and 3.3×10^{-3} psu, respectively (see appendix for details). A light-scattering sensor (LSS) on the CTD platform was not calibrated and instrument voltage anomalies referenced to the observed mean between 1500 and 1850 m are used as the ''nephel'' unit (cf. Thurnherr and Richards 2001).

3. Rift valley hydrography

a. Comparison with published data

Prior to the current-meter deployment a detailed hydrographic survey was carried out in the vicinity of the nontransform discontinuity near 36.25°N (German et al. 1998; Thurnherr and Richards 2001); data from that survey will be referred to as 1997 data to distinguish them from the 1998 data described here. The θ_2/S properties of the pressure-averaged rift valley profiles and of an eastern background station occupied during both surveys are indistinguishable (at the measurement accuracy) below the salinity maximum of the Mediterranean tongue near 1000 m. The water observed in the rift valley (below 2000 m) was therefore most likely of the same origin in both years, that is, inflow from the eastern ridge flank is most likely (Thurnherr and Richards 2001). Inspection of the individual 1998 profiles reveals that the signatures of interleaving of western ridge-flank water, which were common in 1997, are almost entirely absent from the 1998 data (in the two profiles containing such signatures the temperature inversions are of order 5×10^{-3}°C, 20× smaller than those observed in 1997). This is consistent with the flow reversal at 1800 m from northeastward at the beginning of the current-meter records to southwestward toward the end (section 4a).

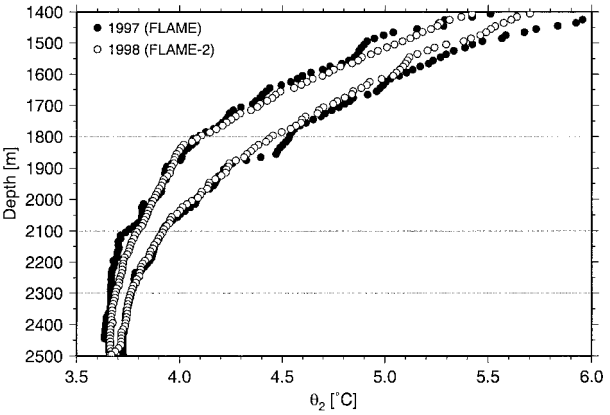

FIG. 2. Comparison of the potential temperatures in the 1997 survey area observed in 1997 and in 1998. Minimum and maximum values are plotted. The horizontal lines indicate the nominal depths of the moored current meters.

In order to assess changes in the rift valley stratification, the temperature, salinity, and density ranges in the common area of the two surveys are compared; Fig. 2 shows the temperature profiles. Data below 2500 m are not plotted because there are only three profiles in this region extending below that depth in the 1998 dataset. The temperature ranges are indistinguishable within the variability encountered during each survey. (The same observation holds for the salinity and for the density data.) The average temperatures recorded by the current meters during the first and the last weeks of deployment indicate net increases ($\pm 1\sigma$) of 0.09(±0.05)°C at 1800 m, 0.14(±0.05)°C at 2100 m, and 0.04(±0.01)°C at 2300 m, that is, less than the variability at the same depths observed during each hydrographic survey. The main horizontal hydrographic pattern observed in 1997 was a cross-sill density gradient related to hydraulically controlled flow from South AMAR into AMAR (Thurnherr and Richards 2001). In the 1998 dataset no similar pattern is apparent, most likely because of the small number of stations occupied near the sill, which does not allow the calculation of representative mean hydrographic profiles.

While these observations indicate that changes between 1997 and 1998 in the rift valley hydrography above 2500 m were small compared to the short-timescale variability, the properties at greater depths may be more revealing because of the small vertical gradients in deep depressions of the rift valley (Saunders and Francis 1985). There is a single CTD repeat station extending to 3200 m from each survey (1.4 km horizontal distance); the corresponding deep θ_2/S properties are shown in Fig. 3. The minimum observed temperatures are 3.655°C (1997) and 3.598°C (1998), implying a cooling of the bottom water of order 0.06°C, a value significantly greater than the CTD temperature calibration uncertainties (see appendix). The temperature strat-

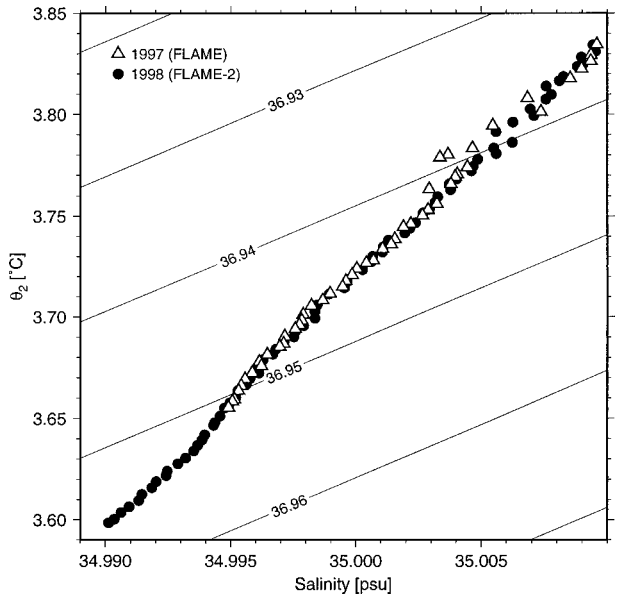

FIG. 3. θ_2/S comparison of 1997 and 1998 profiles in a deep depression near 36.25°N: the 1998 profile is truncated at the maximum depth of the 1997 profile (3200 m); σ_2 contour interval is 0.01.

ifications below 3000 m are $< 5 \times 10^{-5}$ °C m^{-1} in both profiles indicating that neither tidal displacement of the deep isopycnal surfaces (typically 50–100 m, Thurnherr and Richards 2001) nor the difference in bottom depth of the two profiles (60 m) can account for the temperature drop. In conjunction with the warming recorded by the moored sensors this implies a slight increase in the rift valley temperature stratification between 1997 and 1998. The near-perfect agreement between the isothermal salinities apparent in Fig. 3 is fortuitous (typical salinity differences between neighboring profiles of the 1998 dataset are of order 3×10^{-3} psu, consistent with the salinity sensor accuracy).

The 1998 hydrographic data of this study can be compared to published observations in the rift valley near 36.25°N (Table 1). The temperatures recorded in 1981 and in 1994 lie outside the range shown in Fig. 2, indicating that there is some low-frequency variability, possibly caused by changing conditions at the inflow. A comparison of the temperatures and salinities listed in Table 1 with Fig. 3 indicates that all but the 1994 data have mutually indistinguishable θ_2/S characteristics; unfortunately, no information regarding the calibration accuracy is available for the 1994 data. Fehn et al. (1977) conclude that their 1972–74 temperature observations between 36.5° and 37°N are fully consistent with data recorded in the same region in 1959 and in 1964. In section 5 we will make use of the observation that the 1998 temperatures are consistent with 1959 data to infer the most likely pathway of the rift valley water north of AMAR.

TABLE 1. Hydrographic properties at 2470 m in the rift valley near 36.25°N/33.85°W. The 1959 and 1981 data were recorded 6 and 13 km from the location of the repeat station occupied in 1994, 1997, and 1998. The error estimate for the 1959 temperature is associated with visual read-off from a plot.

Year	θ_2	Salinity	Reference
1959	3.72 ± 0.02°C	n/a	Fehn et al. (1977)
1981	3.83°C	35.011 psu	Roemmich and Wunsch (1985)
1994	3.75°C	34.994 psu	German et al. (1996)
1997	3.71°C	34.998 psu	Thurnherr and Richards (2001)
1998	3.69°C	34.999 psu	This study

b. Along-segment hydrographic gradients

In 1998 CTD stations were occupied along the entire length of the two AMAR segments between 35.5° and 36.7°N (Fig. 1). North of 35.9°N the rift valley θ_2/S properties are nearly linear everywhere except at the two stations near 36.25°N where weak interleaving signatures were observed (section 3a). In 7 out of the 12 profiles collected south of 35.9°N there are sharp (≈10-m vertical extent) salinity inversions $\leq 3 \times 10^{-3}$ psu without any apparent signals in the corresponding temperature measurements. In order to characterize the θ_2/S slope variability in the rift valley the profiles with nonlinear θ_2/S properties are removed from the dataset. From the remainder stability ratios $R_\rho = \alpha\theta_z/(\beta S_z)$ (with $\alpha = 1.47 \times 10^{-4}$ °C^{-1} and $\beta = 7.53 \times 10^{-4}$ psu^{-1} at 4°C, 35 psu and 2000 dbar) are calculated from the slopes of linear θ_2/S regressions. Anticipating the possibility of geothermal-heating signatures near the seafloor, separate stability ratios are calculated for two distinct layers. The upper layer is limited above by the 2050-m isobath, the upper limit of the rift valley water at the northern end of the segments (section 5b). The separation depth between the layers of 2300 m is chosen somewhat arbitrarily at the midpoint between the upper limit of the rift valley water and the maximum depth (2550 m) at which hydrographic data from the entire extent of the two segments are available (north of 36.25°N a single profile extends below 2600 m). Because of the small magnitude of the vertical hydrographic gradients at depth only profiles extending below 2550 m are used for the lower-layer estimates. The resulting values are plotted in Fig. 4; the error bars of the individual estimates are derived from the uncertainties of the associated linear θ_2/S fits (setting the a priori uncertainties to the rms salinity-calibration error). The upper-layer stability ratios are approximately constant along the entire length of the two segments with a mean value ($\pm 1\sigma$) of 2.31 ± 0.07 indicating a uniform θ_2/S slope. The northward-decreasing trend in the lower layer is consistent with geothermal heating as discussed in section 7. The gray box shows $R_\rho = 2.25 \pm 0.05$ observed during a 10-h CTD yoyo between 2050 and 2500 m near 36.25°N in 1997 (Thurnherr and Richards 2001). It confirms close

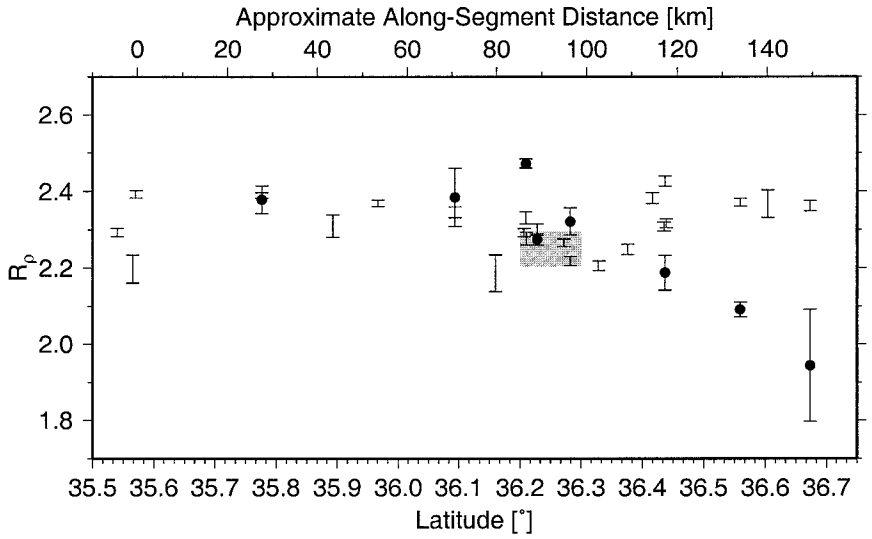

FIG. 4. Rift valley stability ratios: upper-layer values (2050–2300 m) are shown as unmarked error bars; lower-layer values (below 2300 m) are marked with bullets; gray area indicates 1997 CTD-yoyo observations.

agreement between the hydrographic properties observed during the two surveys and indicates the magnitude of the small-scale horizontal variability, which is not included in the error bars of Fig. 4.

The observations of Fehn et al. (1977) and of Saunders and Francis (1985) indicate that monotonic hydrographic along-segment gradients in the rift valley of the MAR are common. Figure 5 shows scatterplots and linear regressions of the temperatures and salinities at 2550 m; the profiles with salinity inversions were not used for the salinity regression. The gradients ($\pm 1\sigma$) and rms errors are $1.0(\pm 0.1) \times 10^{-3}$ °C km^{-1} and 1.2×10^{-2} °C, and $8.5(\pm 1.7) \times 10^{-5}$ psu km^{-1} and 1.4×10^{-3} psu, respectively. The magnitudes of the rms errors are consistent with the temperature variability at periods less than 1 week of 1.3–2.5 ($\times 10^{-2}$ °C) (from the moored instruments at 2300 m). The along-segment density gradient and rms error are $-0.9(\pm 0.2) \times 10^{-4}$ kg m^{-3} km^{-1} and 1.6×10^{-3} kg m^{-3}, respectively. In analogy to the stability ratio a horizontal hydrographic-gradient ratio can be defined as $R_\rho^* = \alpha\theta_x/(\beta S_x)$. Fitting a straight line to the θ_2/S observations at 2550 m yields $R_\rho^* \approx 2.2(\pm 0.4)$. The agreement between R_ρ^* and the mean value of R_ρ implies that no input of heat or salt is required to account for the observed along-segment hydrographic gradients in the rift valley at 2550 m. (The uncertainty associated with the estimate of R_ρ^* allows for some geothermal heating in the rift valley; this, how-

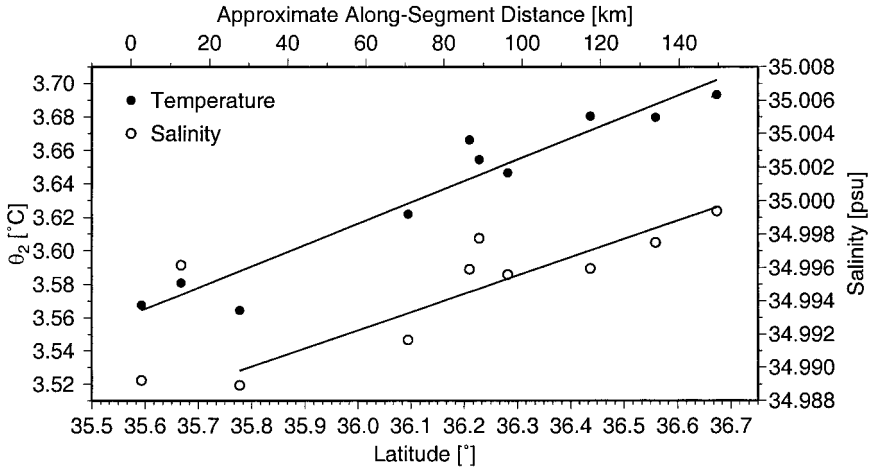

FIG. 5. Scatterplots and linear regressions of the rift valley temperatures and salinities at 2550 m. The two southernmost profiles contain salinity inversions and are not used for the salinity gradient calculation. The regression coefficients ($\pm 1\sigma$) and rms errors are $1.0(\pm 0.1) \times 10^{-3}$ °C km^{-1} and 1.2×10^{-2} °C, and $8.5(\pm 1.7) \times 10^{-5}$ psu km^{-1} and 1.4×10^{-3} psu, respectively.

ever, is not the dominant process giving rise to the along-segment hydrographic gradients; cf. section 5.)

c. Inflow into the rift valley

The hydrographic properties in the rift valley suggest inflow from the eastern ridge flank near the southern end of the segments where the densest water is found close to the deepest sill of the AMAR segments near 35.55°N, 34.2°W. Figure 6 shows a density section from the rift valley side of that sill (small stars in Fig. 1). The total sampling time of the CTD tow-yo is approximately 4 h. The downsloping and spreading of the isopycnal surfaces in the shaded area is qualitatively similar to cross-sill flows elsewhere and consistent with inflow from the southeast. The densest water observed in this section has a σ_2 value of 36.970, which is found at 2200 m in an eastern off-ridge profile located approximately 50 km NE of the sill.

In order to estimate the volume flux into the rift valley the one-and-a-half-layer hydraulic model of Whitehead et al. (1974) is applied as described by Thurnherr and Richards (2001). The relative importance of frictional effects and hydraulic acceleration is assessed by evaluating the nondimensional parameter $P = C_d l/h$ (Pratt 1986), where $C_d(=10^{-3})$, l, and h denote the drag coefficient, the horizontal distance over which the thickness of the active lower layer changes significantly, and the mean thickness of that layer, respectively. (The lowermost isopycnal surface that stays horizontal across the sill is taken as the interface between the two model layers.) Conservatively estimating $l = 5$ km and $h = 300$ m from Fig. 6 results in an estimate for $P \approx 0.02$, indicating that frictional effects can be ignored. The application of the layer model to stratified data requires an estimate for the reduced gravity g', which can be taken from the maximum upstream–downstream density difference in the lower layer (Whitehead 1989). The only upstream CTD station near the sill was occupied ≈3 km SE of the saddle (Fig. 1) and there is some uncertainty as to the depth separating the two model layers and the corresponding value of g'; our estimates are $h_u = 250$–300 m and $g' = 1.8 \times 10^{-4}$ m s^{-2}, respectively. At the inferred interface depth of 1950–2000 m the sill is wide (12 km) compared to the Rossby radius of deformation [$(g'h_u)^{1/2}/f \approx 2.5$ km, where $f = 8.6 \times 10^{-5}$ s^{-1} is the Coriolis parameter at 36°N]. The cross-sill volume-flux estimate becomes $Q = g'h_u^2/(2f) \approx 0.065$–$0.095 \times 10^6$ m^3 s^{-1}, similar to $Q \approx 0.065 \times 10^6$ m^3 s^{-1} calculated from the 1997 data for along-valley flow across the sill near 36.25°N (Thurnherr and Richards 2001).

Not all of the rift valley water must necessarily flow in across a single sill. As discussed in section 3b, a number of the profiles near the southern end of South AMAR contain sharp salinity inversions. The strongest of these signals is found at 2175 m on a station occupied near 35.65°N, 34.35°W (Fig. 1). The high salinity observed there at 2550 m (Fig. 5) indicates that it is the water below the salinity inversion that is anomalous (the θ_2/S properties above the salinity step show no significant offset compared to other rift valley stations). The second-deepest sill near the southern end of South AMAR connects the rift valley to the North Oceanographer segment in the west and the salinity inversions may be signatures of additional inflow across that sill. Any such inflow is most likely small compared to the inflow across the sill shown in Fig. 6 (i) because this sill is approximately 100 m deeper than any other (section 2), and (ii) because the rift valley θ_2/S properties are fully consistent with those observed outside the valley at a station upstream of the sill saddle (the southernmost data point plotted in Fig. 4). Temporal variability at the inflow sill provides an alternative interpretation for the anomalous deep-water properties near the southern end of South AMAR.

4. Current-meter observations

a. 1997 and 1998 flow patterns

Near 36.25°N the rift valley is blocked below 2500 m at a nontransform discontinuity (lateral offset) that separates AMAR from South AMAR. Between June 1997 and June 1998 the flow on the sill and at other nearby locations was monitored by 21 current meters deployed at 1800, 2100, and 2300 m on seven moorings (inset of Fig. 1). On the basis of a hydrographic and LADCP survey Thurnherr and Richards (2001) concluded that during the three weeks prior to mooring deployment the flow below 2000 m across the sill was persistently northeastward and hydraulically controlled. Near the sill no velocity reversals were observed at depth. Vertical isopycnal displacement of 50–100 m consistent with the M_2 period on the other hand indicated the presence of tidal motion.

In order to relate the hydrographic data obtained during the two surveys (24 and 6 days sampling time) to the flow field, average velocities were calculated from the first and from the last weeks of mooring deployment (Fig. 7). The cross-sill flow at 2100 m and at 2300 m was similar in 1997 and 1998 but it reversed direction and increased in strength at 1800 m. The velocities recorded on an additional mooring at 36.43°N (Fig. 1) show NE-ward continuation of the along-valley flow in 1997 with speeds of 0.01–0.03 m s^{-1}, and NE-ward mean flow of 0.02–0.03 m s^{-1} at 2100 and at 2300 m (see also Fig. 10 below) and SW-ward flow of 0.02 m s^{-1} at 1800 m in 1998. The lack of strong interleaving signatures in the 1998 data (section 3a) is consistent with the reversed flow at 1800 m and provides support for the hypothesis of a western origin of the interleaving water (Thurnherr and Richards 2001).

b. Along-segment transport

The strongest currents were recorded by the deep instruments on the sill (Fig. 7) with daily average veloc-

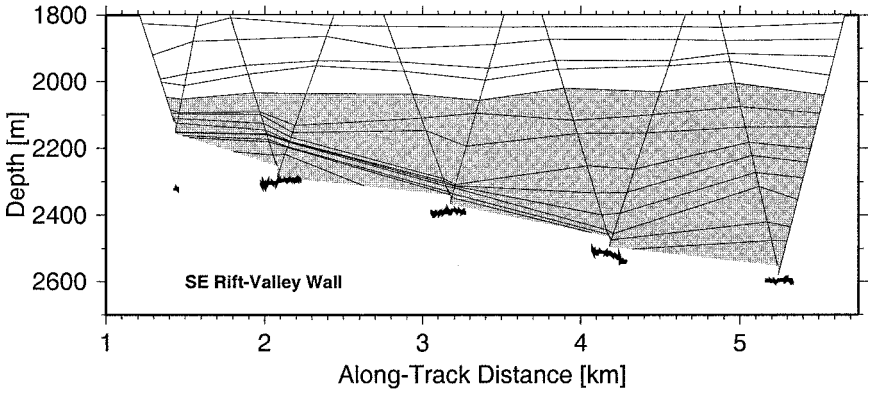

FIG. 6. Density section from the CTD tow-yo on the rift valley side of the sill near 35.55°N, 34.2°W (Fig. 1). Along-track distance increases from SE to NW. The bathymetry is taken from the CTD altimeter. The shaded area indicates $\sigma_2 \geq 36.9449$. Contour levels are selected for uniform spacing with depth in the final upcast.

ities of up to 0.14 m s^{-1}. In order to split the energy into different frequency bands rotary spectral techniques were applied. Similar to observations from midocean ridges elsewhere (e.g., Keller et al. 1975; Mihaly et al. 1998), the spectra show a variety of significant peaks at tidal harmonics (K_1, M_2, M_4, M_6), in the near-inertial band (f), as well as at tidal-inertial nonlinear interaction frequencies ($f + M_2$, $f + M_4$). Additionally, the current-meter records from the AMAR segments contain a variety of oscillations of unclear origin with periods of 3–14 days. [While these frequencies are roughly consistent with free basin modes, the complexity of the terrain allows for a wide range of horizontal scales and the consistency is inconclusive. Topographic Rossby waves can also account for some of the low-frequency oscillations (Thurnherr 2000).]

In all records most of the energy at periods less than 1 week is concentrated in the semidiurnal tidal band, typically exceeding the energy in the diurnal band, which includes the near-inertial frequencies, by about a factor of 4. The velocity variances indicate semidiurnal tidal speeds of 0.03–0.04 m s^{-1}, decreasing slightly with depth. At all periods less than a week, the clockwise (anticyclonic) rotary components dominate with the dominance decreasing with depth, possibly because of increasing lateral confinement by the rift valley walls (topographic steering). On the sill, bottom-intensified low-frequency flow (periods $>$ 1 week) dominates the spectra, accounting for up to 80% of the total energy [see Thurnherr (2000) for additional information].

The current-meter observations (e.g., Fig. 7) suggest that essentially the entire NE-ward along-segment flow below 2000 m crosses the sill where Thurnherr and Richards (2001) inferred hydraulic control in 1997. Therefore, this sill is an ideal location for monitoring the magnitude and variability of the along-segment transport. In order to calculate this transport a valley cross section at the sill (straight lines in Fig. 7) is sep-

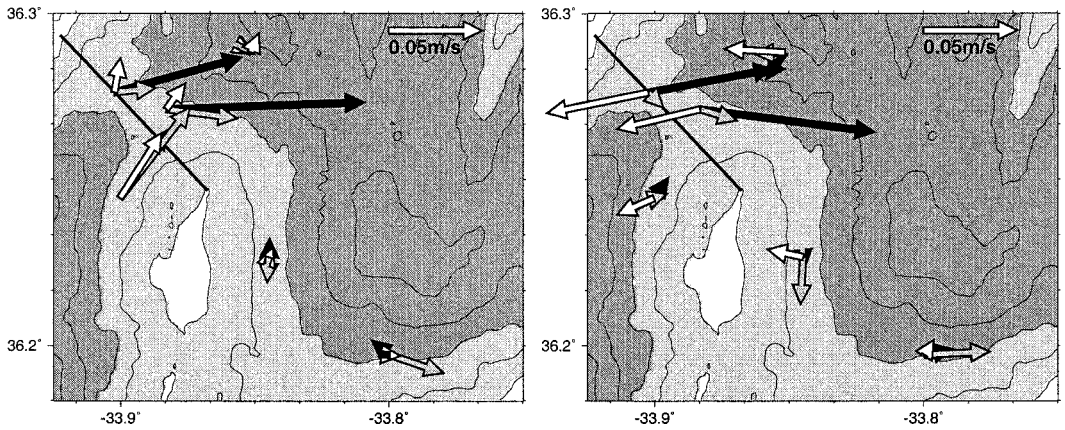

FIG. 7. Average current-meter velocities in the vicinity of the sill connecting the AMAR and the South AMAR segments recorded during (left) the first and (right) the last weeks of mooring deployment; shading of the arrows is determined by the instrument depths with black, gray, and white indicating 2300, 2100, and 1800 m, respectively. Bathymetric shading is the same as in Fig. 1. Contour interval is 250 m. The solid along-sill lines indicate the location of the cross-valley section used to calculate the along-segment transport (cf. Fig. 8).

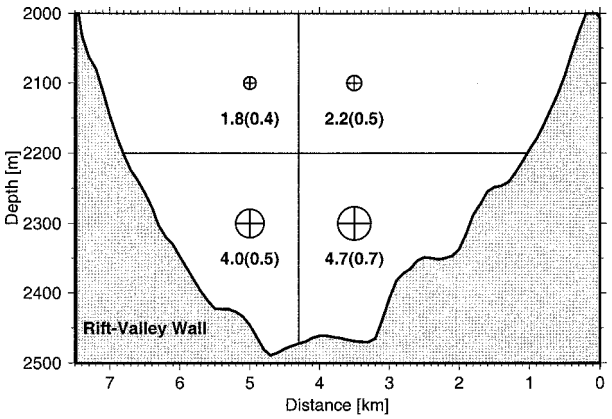

FIG. 8. Cross-valley section on the sill near 36.25°N (straight lines in Fig. 7) and location of the current meters projected onto the section (crossed circles); distance is measured from SE to NW; straight lines indicate subdivision into quadrants for transport calculations. The diameter of the current-meter symbols is proportional to the mean flow speeds normal to the section. In addition to the mean values, uncertainties determined from the spectral properties of the flow (Flierl and McWilliams 1978) are listed in parenthesis below each current meter. Units are 10^{-2} m s^{-1}.

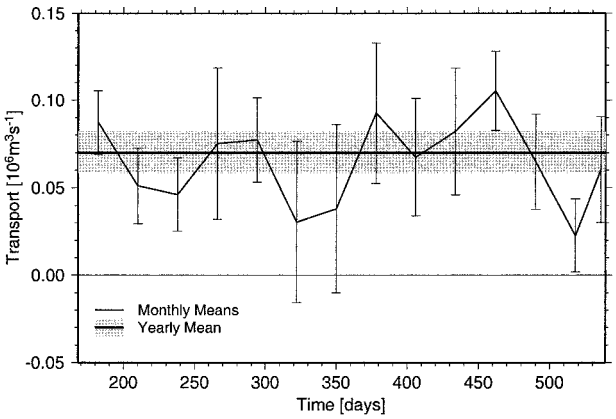

FIG. 9. Monthly and yearly averaged along-valley transport below 2000 m. Monthly error bars show standard deviations of the daily averages. The gray error band of the yearly average corresponds to the uncertainties listed in Fig. 8.

arated into quadrants and the current-meter velocities are projected onto the cross-sill direction, assuming that the observations of each instrument are representative of the mean flow in the corresponding quadrant (Fig. 8). The uncertainties associated with the mean cross-sill speeds shown in parenthesis below each current meter are determined from the spectral properties of the flow (Flierl and McWilliams 1978). In order to estimate the integral timescales required for these error estimates periodic motions are filtered from the along-mean velocities and the resulting lagged autocorrelations are integrated to the first zero crossings. The integral timescales in the overflow range between 10 and 20 days.

In order to assess possible bias the transport calculations are repeated using different methods. A lower bound is calculated by assuming linearly varying flow velocities vanishing at the lateral boundaries and an upper bound is derived from the along-mean velocities (i.e., without projection onto the cross-sectional direction). The resulting estimates indicate an additional uncertainty of 40% in the yearly mean transport. We chose the method shown in Fig. 8 because its solution is characterized by the smallest overall temporal variability (Thurnherr 2000).

Figure 9 shows the monthly and yearly mean cross-sill transports. The error bars of the monthly averages indicate the magnitudes of the standard deviations calculated from the daily transports. The error band of the yearly average (≈17%) is calculated from the uncertainties associated with the mean speeds shown in Fig. 8. While there is considerable daily to monthly variability, the along-segment flow is persistently unidirectional and the yearly averaged transport is well determined by our measurements (i.e., the main energetic timescales are adequately sampled). The good agreement between the hydraulic estimate derived from the 1997 survey (0.065×10^6 m^3 s^{-1}; Thurnherr and Richards 2001) and the current-meter derived yearly ($0.070 \pm 0.012 \times 10^6$ m^3 s^{-1}) and first-month ($0.087 \pm 0.018 \times 10^6$ m^3 s^{-1}) transports significantly increases our confidence in the application of the hydraulic model of Whitehead et al. (1974) (sections 3c and 5b).

5. Mass, heat, and salt budgets

a. Budgets beneath a grounding isopycnal

The observations presented in sections 3 and 4 indicate that the variabilities of the hydrography and of the along-segment transport in the rift valley of the AMAR segments during the current-meter deployment was not high enough to hide a well-defined mean state. In order to proceed we explicitly make a steady-state assumption and treat the variability as random errors. Except near the seabed, the θ_2/S slope of the rift valley water shows no along-segment trend, consistent with the observation that the horizontal hydrographic-gradient ratio R_ρ^* is indistinguishable from the rift valley stability ratio. We anticipate therefore that the along-segment hydrographic gradients are maintained primarily by downward diffusion of heat and salt rather than by geothermal fluxes at the seabed.

Figure 10 shows an along-segment density section in the rift valley between the inflow sill (marked I, section 3c) and the sill which connects the AMAR and FAMOUS segments (marked F), constructed from approximately uniformly spaced stations along the deepest axis of the rift valley. The shaded area indicates water flowing into South AMAR below 2000 m (the lower layer of the hydraulic calculation of section 3c). Apart from sill I the rift valley is closed below 2200 m indicating that lower-layer water is fully blocked by the bathymetry north of ≈35.9°N. The sill at 2200 m connecting

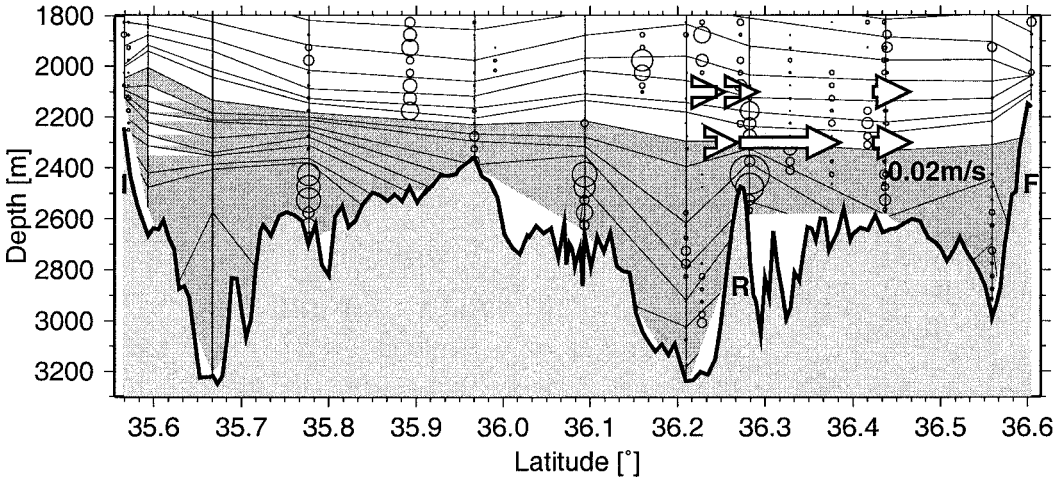

FIG. 10. Rift valley density section (contours), flow speeds (arrows), and diffusivity estimates from overturning scales (''bubbles,'' cf. section 6). The path of the along-segment bathymetry is shown in Fig. 1 (see text for station selection and sill labeling). Density contours are the same as in Fig. 6; the shaded area indicates water with $\sigma_2 \geq 36.9449$. The moorings shown here are marked with bullets in Fig. 1; the lengths of the arrows, measured from the bases of the stems to the tips, show mean along-valley velocities observed during the final week of current meter deployment (cf. Fig. 7).

South AMAR to the North Oceanographer segment (section 2) provides an additional pathway for lower-layer water with both in- and outflow being possible. The salinity inversions observed near the southern end of the segments are consistent with a second, but smaller, source of rift valley water at this sill (section 3c). Transport estimates below 2000 m indicate that the inflow across sill I into South AMAR (section 3c) and the overflow into AMAR across sill R are of similar magnitude (section 4b). We therefore (tentatively) assume that there are no significant additional sources or sinks for the shaded water of Fig. 10, implying that it upwells across the limiting isopycnal in the AMAR segments.

Combining an estimate of the horizontal area enclosed by the 2200-m bathymetric contour (the approximate mean depth of the grounding isopycnal) $A = 2.5(\pm 0.3) \times 10^9$ m^2 with the inflow across sill I [$Q = 0.080(\pm 0.015) \times 10^6$ m^3 s^{-1}; section 3c] yields a mean diapycnal velocity of $3.2(\pm 0.6) \times 10^{-5}$ m s^{-1}.

The heat budget of the shaded layer is given by

$$\rho_0 c_p Q \overline{\Delta\theta} = H_c + H_p + \rho_0 c_p A K_v \theta_z \qquad (1)$$

(e.g., Saunders 1987), where $\overline{\Delta\theta} = 0.11(\pm 0.02)$°C is the mean temperature by which the inflowing water must be heated to cross the grounding isopycnal. (Our estimate of $\overline{\Delta\theta}$ from the CTD tow-yo (section 3c) assumes vertically uniform inflow and yields a lower bound for the heat flux if the cross-sill flow is bottom intensified.) Using reference values for density ($\rho_0 = 10^3$ kg m^{-3}) and specific heat ($c_p = 4.2 \times 10^3$ J kg^{-1} K^{-1}), a flux of $37(\pm 7) \times 10^9$ W must be supplied to the lower layer by a combination of geothermal heating ($H_c + H_p$) and diapycnal mixing. The conductive heat flux $H_c \approx 0.33(\pm 0.03) \times 10^9$ W, calculated from the near-axial heat flow of 131×10^{-3} W m^{-2} (Stein and Stein 1994) combined with the area A of the rift valley at the mean depth of the grounding isopycnal, is insignificant compared to the other terms of the heat budget. A few kilometers upstream of sill R a large hydrothermal vent field supplies $H_p \approx 3(\pm 2) \times 10^9$ W of heat to the rift valley water column (Thurnherr and Richards 2001). Even though the neutrally buoyant hydrothermal particle plume (2000–2300 m) is dispersed above the grounding isopycnal (2300 m near the vent field), it is still possible that the associated heat flux contributes to the budget of the shaded layer both because of entrainment into the buoyant plumes and because of the large diapycnal mixing that is expected to be associated with the overflow from South AMAR into AMAR. Here H_p is an order of magnitude smaller than the total required to balance the budget, however, confirming our hydrographic inference that it is primarily the fluxes caused by mechanical mixing that give rise to the along-segment hydrographic gradients (section 3b). In order to estimate K_v from expression (1) the vertical temperature gradient $\theta_z = 6.2(\pm 3.6) \times 10^{-4}$ °C m^{-1} is calculated from 100-m-thick layers centered at the grounding isopycnal in the deep CTD profiles—the resulting diffusivity estimate becomes $K_v = 5.7(\pm 3.3) \times 10^{-3}$ m^2 s^{-1}.

The salt budget can be written analogously to expression (1) to yield another estimate for K_v (assuming a diffusivity ratio of 1, i.e., neglecting the possibility of double diffusion). By definition there is no contribution of conductive geothermal heating to the salt budget. Converse et al. (1984) estimate mass and heat fluxes from a hydrothermal vent field characterized by source temperatures similar to the ones in the South AMAR vent field (Fouquet et al. 1998). Using their mass:heat

flux ratio yields a mass flux of $\approx 1.5 \times 10^3$ kg s^{-1} at our site. The corresponding salt flux, which is calculated from the source-fluid salinity anomaly of 13 psu (Fouquet et al. 1998), indicates a hydrothermal contribution to the rift valley salt balance of order 2%, well below the uncertainties associated with the other parameters of the salinity analog of expression (1). From the salt budget the diffusivity estimate becomes $K_v = 5.2(\pm 3.1) \times 10^{-3}$ m^2 s^{-1}; that is, it is indistinguishable from the temperature-derived value.

b. Budgets below 2000 m

In order to assess the robustness of the diffusivity estimates calculated in section 5a, separate heat and salt budgets for the water column below 2000 m are derived. The South AMAR estimates for the volume fluxes across sills I (section 3c) and R (section 4) indicate inflow of $0.080(\pm 0.015) \times 10^6$ m^3 s^{-1} and outflow of $0.070(\pm 0.012) \times 10^6$ m^3 s^{-1}, leaving a deficit of $0.010(\pm 0.015) \times 10^6$ m^3 s^{-1}. Interpreting this deficit in terms of upwelling across the 2000-m isobath yields a vertical velocity ($\pm 1\sigma$) of $0.5(\pm 0.8) \times 10^{-5}$ m s^{-1}. In combination with an estimate of the volume of the South AMAR segment the mean residence time of the rift valley water is approximately 5 months.

The AMAR mass budget is more difficult to estimate. The deepest sill near the northern end of the segment connects the rift valley to its northern neighbor at 2200 m (sill F). Northward flow across this sill is therefore taken to be the most likely pathway for the bulk of the water entering AMAR from the south. This is consistent with the persistent strong northeastward flow observed in the rift valley of the FAMOUS segment in 1973 (Keller et al. 1975) as well as with the hydrographic data of Fehn et al. (1977) and of Wilson et al. (1995). Figure 11 shows data from a station occupied directly on sill F. Between 2020 and 2040 m both density and light-scattering profiles are characterized by steep gradients, the corresponding temperature step is ≈ 0.03°C. (In Fig. 10 this pycnocline appears as three isopycnal surfaces nearly coinciding on the sill.) Amazingly, a very similar temperature step (≈ 0.04°C between 2000 and 2025 m) is apparent in a profile taken on the same sill in 1974 [profile 7 in Fig. 4 of Fehn et al. (1977)], suggesting that the pycnocline is a persistent feature, most likely associated with flow across the sill. We take it to mark the interface between two distinct layers. No light-scattering data are available from the rift valley in the FAMOUS segment but the observed signal below the pycnocline on the sill is consistent with water from the AMAR segments where nearly all nephelometry profiles contain weak maxima of 0.01–0.02 V near 2100 m; that is, the data are consistent with eastward lower-layer flow from AMAR into FAMOUS. The θ_2/S properties on the sill (inset in Fig. 11) suggest that the water in the two layers is most likely of the same origin, that is, eastern North Atlantic water. (The slightly different θ_2/S slopes of the two layers may indicate different pathways.) We can also attempt to infer the flow direction below 2000 m across sill F from Fig. 10. The current-meter measurements indicate northward mean flow into the region of the upsloping isopycnal surfaces toward the northern end of the segment. Isopycnal uplifting upstream of sill R was observed in 1997 (Thurnherr and Richards 2001) and the same effect is apparent in Fig. 10. Considering all the indirect evidence, we (tentatively) assume that the flow below the pycnocline shown in Fig. 11 is eastward, in agreement with the conclusion of Fehn et al. (1977).

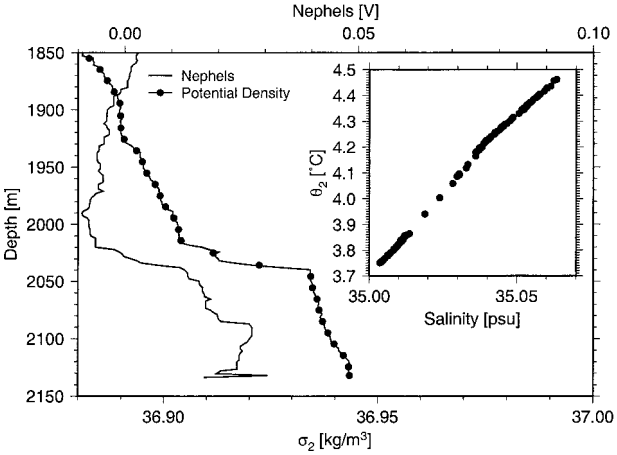

FIG. 11. Hydrographic and light-scattering profiles on sill F connecting the AMAR and FAMOUS segments. In the main panel the potential density and nephelometry (light-scattering) profiles are plotted. The inset shows the corresponding θ_2/S properties.

The volume flux across sill F is calculated with the hydraulic model of Whitehead et al. (1974) (cf. section 3c). Estimating values for the reduced gravity and for the interface height from the center of the pycnocline at 2030 m yields $g' = 3 \times 10^{-4}$ m s^{-2} and $h_u = 170$ m (from the altimeter). The corresponding Rossby radius of deformation (2.6 km) is less than the sill width at 2000 m (5 km) indicating that the hydraulic model can be applied as before. The volume-flux estimate becomes $0.05 \pm (0.01) \times 10^6$ m^3 s^{-1}, assuming that the relative uncertainty is similar to that at the inflow (section 3c). Together with the estimate for the flow across sill R [$0.070(\pm 0.012) \times 10^6$ m^3 s^{-1}; section 4b] the AMAR volume budget is characterized by a deficit of $0.02(\pm 0.01) \times 10^6$ m^3 s^{-1}. Interpreting this deficit in terms of upwelling across the 2000-m isobath yields a vertical velocity ($\pm 1\sigma$) of $2.0(\pm 1.0) \times 10^{-5}$ m s^{-1}. In combination with an estimate of the volume of the AMAR segment the mean residence time of the rift valley water is approximately three months.

Using the mass budgets of the two segments, we can derive independent estimates for the diapycnal fluxes across the 2000-m isobath. Redefining Q and $\overline{\Delta\theta}$ of expression (1) to denote the average along-segment

transports and the mean temperature differences between the segment in- and outflows, respectively, and estimating the corresponding isobaric values for A and θ_z, the same expression (as well as its salinity analog) describes the heat (salt) budget below 2000 m. (This implicitly treats the mass-balance deficits as fluxes associated with the mean segment temperatures and salinities; i.e., we assume that they do not contribute to the heat and salt balances.) The heat flux of the hydrothermal vent field contributes approximately 5% to the South AMAR balance. If it is assumed that the uncertainties associated with the vertical-gradient estimates (here ≈50%) dominate the diffusivity errors, the resulting K_v estimates for South AMAR are $4.1(\pm 1.9) \times 10^{-3}$ m^2 s^{-1} (heat) and $4.3(\pm 2.2) \times 10^{-3}$ m^2 s^{-1} (salt), and those for AMAR are $3.0(\pm 1.4) \times 10^{-3}$ m^2 s^{-1} (heat) and $7.5(\pm 3.9) \times 10^{-3}$ m^2 s^{-1} (salt).

Possible errors not considered in the formal uncertainties of these diffusivity estimates include additional source and sink terms in the volume budgets as well as uncertainties in the hydrographic estimates, especially at sill F where all values are derived from a single CTD station. The observation that all diffusivity estimates are of the same order suggests, however, that the tentative assumptions that were required in order to calculate the budgets are at least approximately correct.

6. Diffusivity estimates from overturning scales

While the mutual consistency of the diffusivities derived from hydrographic budgets (section 5) is encouraging, no information about the spatial distribution of the mechanical mixing taking place in the rift valley is obtained. A number of studies have shown that there is a correlation between overturning scales estimated from density-sorted hydrographic profiles [called Thorpe scales, after Thorpe (1977)] and diffusivity estimates derived from microstructure profiles (e.g., Dillon 1982; Ferron et al. 1998); that is,

$$\overline{K_v} \approx \gamma \overline{N L_T^2}, \tag{2}$$

where $\gamma \approx 0.2$ is the product of an empirical factor of ≈0.95 [called a in Ferron et al. (1998)] and the mixing efficiency $\Gamma \approx 0.2$, N is the buoyancy frequency, and L_T is defined as the rms of the Thorpe displacements of individual overturns. Because the correlation between K_v and L_T^2 is associated with large scatter, spatial averaging (indicated by overbars) is used to estimate diapycnal diffusivities from Thorpe displacements. We are interested primarily in order-of-magnitude diffusivity estimates and the (qualitative) spatial distribution of mixing; we therefore do not analyze individual overturns but estimate L_T as the rms of the Thorpe displacements and the corresponding stratifications in 50-dbar bins. Inspection of individual profiles indicates that the salinity stratification below ≈2500 m is too weak to be resolved at smaller overturning scales. Therefore, N is calculated from temperature data and the mean rift valley stability ratio $R_\rho = 2.31$ (section 3b); that is,

$$N^2 = g\alpha(1 - R_\rho^{-1})\theta_z. \tag{3}$$

The underlying assumption of linear θ_2/S characteristics implies that no diffusivities are estimated from the profiles containing interleaving signatures and salinity inversions (section 3).

In order to separate real overturns from false ones caused by measurement scatter the magnitude of the CTD-temperature-sensor fluctuations has to be estimated. Visual inspection of profiles extending below 3000 m indicates that the temperature noise in the 2dbar-averaged profiles is approximately 2×10^{-4} °C; we use values between zero and 10^{-3} °C to assess the sensitivity of the resulting diffusivities to variations of this parameter. Several different methods have been proposed to separate true from noise-related overturns. We use both the criterion of Thorpe (1977) (displacements are considered true if the sorted profile differs by more than the measurement uncertainty from the observed profile) and the algorithm of Ferron et al. (1998) (the observed profile is prerounded to multiples of the noise level with the direction of rounding determined by the previous value in the rounded profile so as to minimize the fluctuations).[1]

Figure 10 shows the rift valley distribution of the diffusivity estimates as ''bubbles'' (with areas proportional to the 50-dbar averages) calculated with the algorithm of Ferron et al. (1998) and assuming an instrument noise of 2×10^{-4} °C. [Qualitatively, the same distribution is obtained regardless of the value of the instrument noise and also with the method of Thorpe (1977).] All stations with linear θ_2/S properties are shown, except for one near 36.2°N (the southernmost station shown in the inset of Fig. 1), which would appear upstream of sill R, but which is downstream in the sense of the mean flow. The diffusivity profile of the omitted station is characterized by very large values near 2000 m (only slightly below the largest ones shown in Fig. 10). The profiles near 35.9° and 36.15°N are both located over topographic highs (Fig. 1); that is, the large diffusivities observed there extend all the way to the seabed. Apart from these two profiles most areas of high diffusivities (including the one not shown) are found downstream of topographic obstacles

[1] In an implementation provided by B. Ferron the intermediate profile is calculated as follows (using the notation of Ferron et al. (1998) and setting the arbitrary constant $T_0 = 0$):

$$TI_1 = \delta\left\lceil \frac{TR_1}{\delta} \right\rceil; \qquad TI_{k+1} = TI_k + \delta \mathcal{F}\left(\frac{TR_{k+1} - TI_k}{\delta}\right),$$

where

$$\mathcal{F}(x) = \begin{cases} \lfloor x \rfloor & \text{if } x \geq 0 \\ \lceil x \rceil & \text{otherwise} \end{cases}$$

(called FIX in Matlab) rounds x to the nearest integer toward zero.

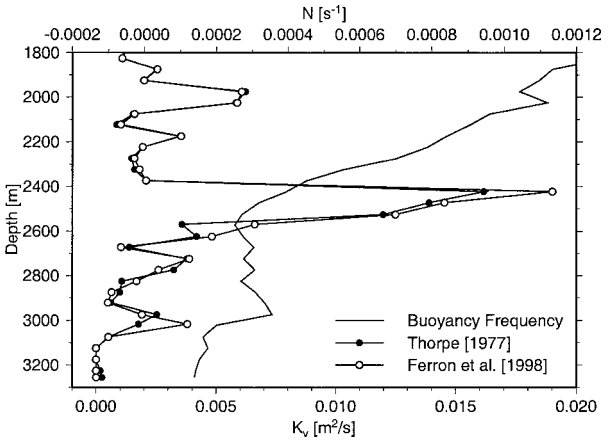

FIG. 12. Ensemble-averaged rift valley buoyancy-frequency and diffusivity estimates from Thorpe displacements using two different methods to account for the instrument noise (2×10^{-4} °C).

in the path of the mean flow. It is interesting to note that the largest values occur just downstream of sill R where Thurnherr and Richards (2001) inferred hydraulic control.

The distribution of the diffusivities shown in Fig. 10 indicates that the spatial (and most likely temporal) variability is not well sampled. Nevertheless a horizontally averaged diffusivity profile is shown together with the corresponding buoyancy frequencies in Fig. 12. The main signal is the maximum at 2400–2600 m. Below this peak the diffusivity profile is strongly dependent on the assumed instrument noise level whereas it is robust above 2400 m. The maximum near 2500 m is reduced by approximately 35% when the instrument noise level is increased to 10^{-3} °C. On the other hand, the peak value is approximately doubled when ensemble-averaged buoyancy-frequencies are used in expression (2) instead of the stratifications calculated from the individual density-sorted profiles, implying that the main overturns are associated with below-average stratifications. Except for the main peak near 2500 m the methods of Thorpe (1977) and of Ferron et al. (1998) yield indistinguishable results. Within the peak the method of Thorpe (1977) is somewhat more conservative with the difference increasing with increasing assumed instrument noise; at a noise level of 10^{-3} °C the peak values are 8.6×10^{-3} m^2 s^{-1} [Thorpe (1977) algorithm] and 12.5×10^{-3} m^2 s^{-1} [Ferron et al. (1998) algorithm].

Figure 12 indicates a diffusivity of $\approx 6 \times 10^{-3}$ m^2 s^{-1} near 2000 m, in excellent agreement with the budget-derived estimates (section 5b). The magnitude of the diffusivity maximum near 2000 m is strongly dependent on the inclusion of a single profile from a station occupied downstream of a topographic high rising to 1950 m (inset of Fig. 1) where Thurnherr and Richards (2001) observed large topographic lee waves, however. When that profile (which is not shown in Fig. 10) is removed from the dataset the peak value drops to 2–3 $\times$ 10^{-3} m^2 s^{-1}; that is, the overturn-derived diffusivity estimates still agree with the budget-derived values within a factor of 2–3.

7. Discussion

In 1998 the rift valley hydrography of the AMAR segments was characterized by monotonically NE-ward increasing temperatures [similar to observations elsewhere on the MAR (Fehn et al. 1977; Saunders and Francis 1985)] and salinities, and by an overall decrease in density. The consistency with published hydrographic data from the same area collected between 1959 and 1997 suggests that the 1998 observations are representative of a long-term persistent state. The rift valley θ_2/S characteristics indicate inflow from the eastern ridge flank as the main source of the rift valley water. A density section from the deepest sill of the AMAR segments, near the southern end where the densest water is observed, is consistent with such an inflow. Approximately 100 km downstream of the inflow unidirectional NE-ward along-segment flow was observed during an entire year. There is evidence for similar unidirectional flow in the same region in 1994, 1996, and 1997 (Thurnherr and Richards 2001). The unidirectional NE-ward flow observed in the FAMOUS segment in 1973 (Keller et al. 1975) is consistent with continuation of the along-valley flow. These observations imply that the ventilation of the AMAR segments is unlikely to take place as inflow events alternating with quiet periods of homogenization (Saunders and Francis 1985). [The simple analytical and numerical model of Thurnherr (2000) shows that a sequence of basins connected by sills—a crude representation of the rift valley—can act as an efficient low-pass filter. This provides a plausible explanation for the persistence of the along-valley flow in spite of the observation of bottom-water cooling of $\approx$0.06°C in the course of 1 yr, which may indicate time-varying conditions at the inflow.]

The rift valley density decreases along the path of the mean flow while the segment-scale variation in the θ_2/S slope is of the same order as the small-scale temporal and spatial variability, indicating that the streamwise hydrographic gradients are primarily caused by mechanical mixing, consistent with the observation that the value of the horizontal hydrographic-gradient ratio R_ρ^* is similar to the mean rift valley stability ratio R_ρ. The northward trend toward lower values of R_ρ below 2300 m is most likely caused by geothermal heating slightly reducing the weak temperature stratification (of order 10^{-4} °C m^{-1}). Taking the θ_2/S properties of the upper layer as a reference, the near-bottom temperature anomalies in the north of the segment are of order 5×10^{-3} °C. Both direct input at the seabed (e.g., by low-temperature hydrothermal sources), and downward diffusion of the heat released into the water column at the hydrothermal vent field near 36.25°N

may contribute to the near-bottom along-stream trend. The mutual consistency of the diffusivities calculated from heat and salt budgets implies that the total geothermal heat flux in the AMAR segments (conductive, high-, and low-temperature) is of the same order as the value calculated from the hydrographic anomalies associated with the hydrothermal particle plume (Thurnherr and Richards 2001); that is, it is unlikely that the plume-derived heat flux is significantly lower than the total because of low-temperature hydrothermal effluents, which are not entrained into the particle plume (e.g., Ginster et al. 1994).

The available bathymetric datasets [see also Fig. 7 of Fehn et al. (1977)] indicate that the rift valley north of the sill connecting South AMAR to AMAR is closed below 2000 m, with the exception of a sill between 2000 and 2100 m on the eastern rift valley wall of the FAMOUS segment near 36.4°N, 32.9°W. The bulk of the mean along-valley flow below 2000 m must therefore upwell within the rift valley, which is consistent with the high diapycnal velocity of $\approx 3 \times 10^{-5}$ m s^{-1} estimated for the deep rift valley. The vertical velocity estimates of $0.5–2 \times 10^{-5}$ m s^{-1} across the 2000-m isobath indicate that some of the water may leave the rift valley by upwelling over a range of densities. This ''diffuse'' three-dimensional pathway may partially explain why large-scale geochemical signatures of the hydrothermal sources known to exist on the MAR have been much harder to detect than the corresponding signatures near faster spreading ridges (without deep rift valleys) in the Pacific, where the hydrothermal plumes rise above the blocking topography and probably act as more focused sources, spreading in two dimensions. (The terms ''focused'' and ''diffuse'' used here should not be confused with the same terms applied to hydrothermal venting styles.)

The along-stream density gradient implies a high rate of mechanical mixing in the rift valley. Diffusivity estimates calculated from heat and salt budgets as well as those derived from overturning scales yield values near 5×10^{-3} m^2 s^{-1}; that is, 500× higher than typical values observed in the main thermocline (e.g., Munk and Wunsch 1998) [and 50× higher than the ''canonical'' value of Munk (1966)]. A similar monotonic along-valley density gradient has been observed in a canyon on the western flank of the MAR in the South Atlantic, where both direct (St. Laurent et al. 2001) and indirect (Ledwell et al. 2000) estimates indicate near-bottom diapycnal diffusivities of order 10^{-3} m^2 s^{-1}. There are two mechanisms that can account for such high mixing rates. From the spatial distribution of microstructure measurements Polzin et al. (1997) inferred that enhanced mixing over the rough western flank of the MAR in the South Atlantic is related to breaking internal waves. Both hydrographic (Thurnherr and Richards 2001) and current-meter observations in the AMAR segments show signatures of energetic internal waves. The large diffusivities observed over topographic highs in the rift valley are consistent with this process. The second mechanism that can account for the observed mixing rates is the vertical shear (and possibly also hydraulic jumps) associated with flows across sills (e.g., Wesson and Gregg 1994; Ferron et al. 1998). In the rift valley of the AMAR segments there is hydrographic evidence for several such overflows. The spatial distribution of the diffusivity maxima in the rift valley suggests that much of the mixing may be associated with these cross-sill flows as the water spills from deep basin to deep basin. This conceptual model implies a complex interplay between mixing, internal waves, cross-sill flows, and upwelling. Without diapycnal mixing dense water would fill the valley and eventually flood the control at the inflow. In order to achieve a steady state with nonzero flow the cross-sill density gradients must be maintained by buoyancy fluxes downstream of the sills. Our data suggest that the geothermal fluxes are insignificant in comparison to mechanical mixing, even in the presence of a large hydrothermal vent field. Therefore, it appears that the diapycnal mixing associated with the overflows themselves contributes substantially to the maintenance of the cross-sill pressure gradients.

The bathymetry of many sub-marine valleys can be crudely represented as a sequence of basins connected by sills. On midocean ridges these include rift valleys, fracture zones, and transform faults, as well as canyons on ridge flanks. A number of hydrographic sections indicate monotonic along-valley gradients in such settings (Fehn et al. 1977; Saunders and Francis 1985; Wilson et al. 1995; Ferron et al. 1998; Ledwell et al. 2000). Therefore, it seems likely that results from our study can be applied elsewhere. Important questions regarding the energetics of valley flows and the interplay between different processes have not been answered here and merit further study. Therefore, we will not yet attempt to assess the potential significance of such flows for the global mixing budget but note that the topographically rough MAR alone accounts for about one-third of the global midocean ridge system.

Acknowledgments. We thank the RVS technical team P. Taylor and P. Howarth and the officers and crew of FS *Poseidon* for their support during the acquisition of the data presented here. Bruno Ferron kindly provided an implementation of his Thorpe-scale algorithm. The issues raised by two anonymous reviewers helped us clarify a number of points. This work was primarily funded by ECMAST (III) project ''AMORES'' (Contract MAST3-CT95-0040) and by a NERC grant (SOC Shiptime Award) with further support for one of the authors (A.M.T.) from a studentship of the University of Southampton and UNESCO. Additional analysis was carried out in the context of the WOCE AIMS Deep Basin Experiment Synthesis project (NSF Grant OCE-9911148).

APPENDIX

Sensor Calibration

Because of instrument problems, two separate Neil-Brown Mk.IIIb CTDs were used on a platform also equipped with a Sea Tech Light Scattering Sensor, a 12-bottle sampling rosette, and auxiliary instruments such as an altimeter. The temperature sensor of one of the two CTDs was precruise calibrated (the other instrument had been taken as a spare). In order to calibrate the temperature sensors, the first sampling bottle of the CTD rosette was fitted with two digital reversing thermometers, precruise calibrated to $\pm 2 \times 10^{-3}$ °C. Near-bottom temperatures were recorded at 23 CTD stations. The average of the two thermometer readings was used for calibration. Rms errors of the temperature calibrations for the two CTDs are 1.2×10^{-3} °C and 1.5×10^{-3} °C, respectively. The conductivity sensors of both CTDs were calibrated by analyzing 34 and 158 bottle samples with an Ocean Scientific International AUTOSAL Model 8400A salinometer, resulting in rms errors of 1.8×10^{-3} psu and 3.3×10^{-3} psu, respectively. The nominal conductivity sensor accuracy of 5×10^{-6} S m^{-1} corresponds to a salinity accuracy of 6×10^{-3} psu at 4°C and 3000 dbar.

The 21 Aanderaa RCM 8 current meters recorded data at hourly intervals between July 1997 and July 1998. The nominal depths of the instruments, all of which had temperature sensors installed, are 1800, 2100, and 2300 m. The central current meters on each mooring were fitted with *Sea Tech* LSS, and some of the instruments had pressure and/or conductivity sensors installed. All LSS and all but one of the conductivity sensors failed with indications for cross-contamination of the pressure signals. None of the pressure data show any correlated shifts or trends recorded by multiple instruments on a single mooring. Therefore, the nominal depths of the instruments are used in the analysis. Velocity and temperature data from all instruments were recovered successfully without any indication of contamination. Flow speeds and directions were sampled every 72 s and vector-averaged before storage; spot measurements were recorded from the remaining sensors. Total common record length is 372 days (53 weeks and 1 day).

The current-meter compasses were calibrated before and after the deployment period at 10° intervals; because of the procedure, differences between the two calibrations (nowhere greater than 10°) are more likely to be errors than temporal shifts (P. G. Taylor 2000, personal communication)—therefore, the more self-consistent of the two calibrations (based on a comparison of neighboring calibration points) was applied. The calibrated directions were then corrected for magnetic declination (−15°) at 36.25°N, 33.9°W on 1 January 1998 (IAGA Division V Working Group 8, 1995). The temperature sensors of the current meters were calibrated both before and after the deployment period; a number of the post-deployment calibrations were erroneous and were therefore repeated. The pre- and the corrected postdeployment calibrations differ by up to 0.5°C without indications for similar shifts in the data but most are 0.03°C or less. Because the quality of the calibrations is somewhat doubtful and because the temperature records do not show any recognizable trends or discontinuities that could be corrected by taking the pre- to postdeployment calibration differences into account, we decided to individually apply the calibrations, which minimize the differences between the mean hydrography sampled during the 1997 cruise (which contains >200 profiles in the current-meter region) and the mean temperatures calculated from the first week of each current-meter record. Because of the variability of the hydrography on tidal timescales (Thurnherr and Richards 2001) no attempt was made to relate the temperature records to individual CTD profiles. The calibrated current-meter temperatures are all low-biased with respect to the CTD temperatures with offsets between -5×10^{-2} °C and -8×10^{-2} °C.

REFERENCES

Adcroft, A., J. R. Scott, and J. Marotzke, 2001: Impact of geothermal heating on the global ocean circulation. *Geophys. Res. Lett.*, **28,** 1735–1738.

Converse, D. R., H. D. Holland, and J. M. Edmond, 1984: Flow rates in the axial hot springs of the East Pacific Rise (21°N): Implications for the heat budget and the formation of massive sulfide deposits. *Earth Planet. Sci. Lett.*, **69,** 159–175.

Detrick, R. S., H. D. Needham, and V. Renard, 1995: Gravity anomalies and crustal thickness variations along the Mid-Atlantic Ridge between 33°N and 40°N. *J. Geophys. Res.*, **100,** 3767–3787.

Dillon, T. M., 1982: Vertical overturns—A comparison of Thorpe and Ozmidov length scales. *J. Geophys. Res.*, **87,** 9601–9613.

Fehn, U., M. D. Siegel, G. R. Robinson, H. D. Holland, D. L. Williams, A. J. Erickson, and K. E. Green, 1977: Deep-water temperatures in the FAMOUS area. *Geol. Soc. Amer. Bull.*, **88,** 488–494.

Ferron, B., H. Mercier, K. Speer, A. Gargett, and K. Polzin, 1998: Mixing in the Romanche Fracture Zone. *J. Phys. Oceanogr.*, **28,** 1929–1945.

Flierl, G. R., and J. C. McWilliams, 1978: On the sampling requirements for measuring moments of eddy variability. *J. Mar. Res.*, **35,** 797–820.

Fouquet, Y., and Coauthors, 1998: FLORES diving cruise with the Nautile near the Azores—First dives on the Rainbow field: Hydrothermal seawater/mantle interaction. *InterRidge News*, **7,** 24–28.

German, C. R., G. P. Klinkhammer, and M. D. Rudnicki, 1996: The Rainbow hydrothermal plume, 36°15′N, Mid-Atlantic Ridge. *Geophys. Res. Lett.*, **23,** 2979–2982.

——, K. J. Richards, M. D. Rudnicki, M. M. Lam, J. L. Charlou, and the FLAME Scientific Party,1998: Topographic control of a dispersing hydrothermal plume. *Earth Planet. Sci. Lett.*, **156,** 267–273.

Ginster, U., M. J. Mottl, and R. P. Von Herzen, 1994: Heat flux from black smokers on the Endeavor and Cleft segments, Juan de Fuca Ridge. *J. Geophys. Res.*, **99,** 4937–4950.

IAGA Division V Working Group 8, 1995: International geomagnetic field, 1995 revision. *J. Geomagn. Geoelectr.*, **47,** 1257–1261.

Jean-Baptiste, P., H. Bougault, A. Vangriesheim, J. L. Charlou, J. Radford-Knoery, Y. Fouquet, D. Needham, and C. German,

1998: Mantle ^{3}He in hydrothermal vents and plume of the Lucky Strike site (Mid-Atlantic Ridge 36°17′N) and associated geothermal heat flux. *Earth Planet. Sci. Lett.,* **157,** 69–77.

Keller, G. H., S. H. Anderson, and J. W. Lavelle, 1975: Near-bottom currents in the Mid-Atlantic Ridge rift valley. *Can. J. Earth Sci.,* **12,** 703–710.

Ledwell, J. R., E. T. Montgomery, K. L. Polzin, L. C. St. Laurent, R. W. Schmitt, and J. M. Toole, 2000: Evidence for enhanced mixing over rough topography in the abyssal ocean. *Nature,* **403,** 179–182.

Lukashin, V. N., A. P. Lisitzin, G. V. Ivanov, V. A. Kravtsov, and V. Rusakov, 1995: The southern hydrothermal plume at the Broken Spur vent field, 29°N (BRAVEX-94). *BRIDGE Newslett.,* **9,** 20–23.

McDougall, T. J., 1990: Bulk properties of ''hot smoker'' plumes. *Earth Planet. Sci. Lett.,* **99,** 185–194.

Mihaly, S. F., R. E. Thomson, and A. B. Rabinovich, 1998: Evidence for nonlinear interaction between internal waves of inertial and semidiurnal frequency. *Geophys. Res. Lett.,* **25,** 1205–1208.

Munk, W., 1966: Abyssal recipes. *Deep-Sea Res.,* **13,** 707–730.

——, and C. Wunsch, 1998: Abyssal recipes II: Energetics of tidal and wind mixing. *Deep-Sea Res.,* **45,** 1977–2010.

Murton, B. J., L. J. Redbourn, C. R. German, and E. T. Baker, 1999: Sources and fluxes of hydrothermal heat, chemicals and biology within a segment of the Mid-Atlantic Ridge. *Earth Planet. Sci. Lett.,* **171,** 301–317.

Needham, H. D., M. Voisset, V. Renard, H. Bougault, O. Dauteuil, R. Detrick, C. Langmuir, and Anonymous,1992: Structural and volcanic features of the Mid-Atlantic Rift Zone between 40°N and 33°N. *Eos Trans. Amer. Geophys. Union,* **73** (Suppl.), F552.

Parson, L., E. Gracia, D. Coller, C. German, and D. Needham, 2000: Second-order segmentation; the relationship between volcanism and tectonism at the Mid-Atlantic Ridge, 38°N–35°40′N. *Earth Planet. Sci. Lett.,* **178,** 231–251.

Polzin, K. L., J. M. Toole, J. R. Ledwell, and R. W. Schmitt, 1997: Spatial variability of turbulent mixing in the abyssal ocean. *Science,* **276,** 93–96.

Pratt, L. J., 1986: Hydraulic control of sill flow with bottom friction. *J. Phys. Oceanogr.,* **16,** 1970–1980.

Roemmich, D., and C. Wunsch, 1985: 2 transatlantic sections—Meridional circulation and heat-flux in the sub-tropical North-Atlantic Ocean. *Deep-Sea Res.,* **32,** 619–664.

Rudnicki, M. D., R. H. James, and H. Elderfield, 1994: Near-field variability of the TAG non-buoyant plume, 26°N, Mid-Atlantic Ridge. *Earth Planet. Sci. Lett.,* **127,** 1–10.

Saunders, P. M., 1987: Flow through Discovery Gap. *J. Phys. Oceanogr.,* **17,** 631–643.

——, and T. J. Francis, 1985: The search for hydrothermal sources on the Mid-Atlantic Ridge. *Progress in Oceanography,* Vol. 14, Pergamon Press, 527–536.

Smith, W. H. F., and D. T. Sandwell, 1997: Global seafloor topography from satellite altimetry and ship depth soundings. *Science,* **277,** 1957–1962.

St. Laurent, L. C., J. M. Toole, and R. W. Schmitt, 2001: Buoyancy forcing by turbulence above rough topography in the abyssal Brazil Basin. *J. Phys. Oceanogr.,* **31,** 3476–3495.

Stein, C. A., and S. Stein, 1994: Constraints on hydrothermal heat-flux through the oceanic lithosphere from global heat-flow. *J. Geophys. Res.,* **99,** 3081–3095.

Thorpe, S. A., 1977: Turbulence and mixing in a Scottish loch. *Philos. Trans. Roy. Soc. London,* **A286,** 125–181.

Thurnherr, A. M., 2000: Hydrography and flow in the rift valley of the Mid-Atlantic Ridge. Ph. D. thesis, University of Southampton, 141 pp.

——, and K. J. Richards, 2001: Hydrography and high-temperature heat flux of the Rainbow hydrothermal site (36°14′N, Mid-Atlantic Ridge). *J. Geophys. Res.,* **106,** 9411–9426.

Wesson, J. C., and M. C. Gregg, 1994: Mixing at Camarinal Sill in the Strait of Gibraltar. *J. Geophys. Res.,* **99,** 9847–9878.

Whitehead, J. A., 1989: Internal hydraulic control in rotating fluids—Applications to oceans. *Geophys. Astrophys. Fluid Dyn.,* **48,** 169–192.

——, A. Leetmaa, and R. A. Knox, 1974: Rotating hydraulics of straits and sill flows. *Geophys. Fluid Dyn.,* **6,** 101–125.

Wilson, C., K. Speer, J.-L. Charlou, H. Bougault, and G. Klinkhammer, 1995: Hydrography above the Mid-Atlantic Ridge (33°–40°N) and within the Lucky Strike segment. *J. Geophys. Res.,* **100,** 20 555–20 564.